SIMULATION AND ANALYSIS OF MULTI-INPUT DC-DC CONVERTER WITH FUZZY CONTROL BASED HYBRID ENERGY STORAGE SYSTEMS IN ELECTRIC VEHICLES

Karla Satheesh[1], Ch.Divya Krishna[2], Gopala Venu Madhav[3]
[1]M.Tech (PEED), Anurag Group of Institutions
[2]M.Tech (PEED), Anurag Group of Institutions
[3]Professor, Dept. of EEE, Anurag Group of Institutions

ABSTRACT

A new multi-input dc–dc boost converter with fuzzy control based upon the hybrid energy system is proposed in this paper. In this paper we are using fuzzy controller comparing to other controller due to some advantages. The fuzzy controller is the most suitable for the human decision-making mechanism, providing the operation of an electronic system with decisions of experts. The proposed converter can be used for transferring energy between different energy resources. The proposed converter operation classified into two modes i.e. Battery charging mode and battery discharging mode. In charging mode main energy system supplies to load and also delivers power to the rechargeable energy storage systems and in discharging mode all input sources deliver power to output. The proposed converter is used for controlling the power of ESSs by allowing active power sharing. The voltage levels of utilized ESSs can be higher or lower than the output voltage. By using the fuzzy controller for a nonlinear system allows for a reduction of uncertain effects in the system control and improves the efficiency. By using the simulation results we can analyze the novel bidirectional non-isolated multi-input converter (MIC) topology for hybrid systems to be used in electric vehicles.

Index Terms: Batteries, bidirectional, hybrid energy storage systems, ultra-capacitors, Fuzzy controller, multi-input converter.

I. INTRODUCTION

The large number of automobiles in use around the world has caused and continues to cause serious problems of environment and human life. Due to reduction of air pollution Electric Vehicles (EVs), Hybrid Electric Vehicles (HEVs) and Fuel Cell Electric Vehicles (FCEVs) have been proposed to replace conventional vehicles. The main objective of HESS(Hybrid energy storage system) is having the characteristics of an ideal energy storage unit such as high energy/power density, low cost/weight per unit capacity, and long cycle life, hybridized batteries and ultracapacitors (UCs). HESS can be classified into two main categories, i.e., isolated and non-isolated. Comparing to isolated, non isolated power converters are much simpler in terms of design and control.

The renewable energy sources and battery have different voltage levels, so to provide a specific voltage level for load and control power flow between input sources, dc-dc converter is required. To control the output voltage multiple converter topology is used. The cost for multiple converter is high, to decrease the cost of multiple converter topologies, multi input converter (MIC) topologies are proposed. MICs are reliable, simple, and easy to control. In a bidirectional MIC having a single inductor shared by input sources is proposed; although this converter has the advantage of being simple, unfortunately, it does not allow active power sharing between sources.
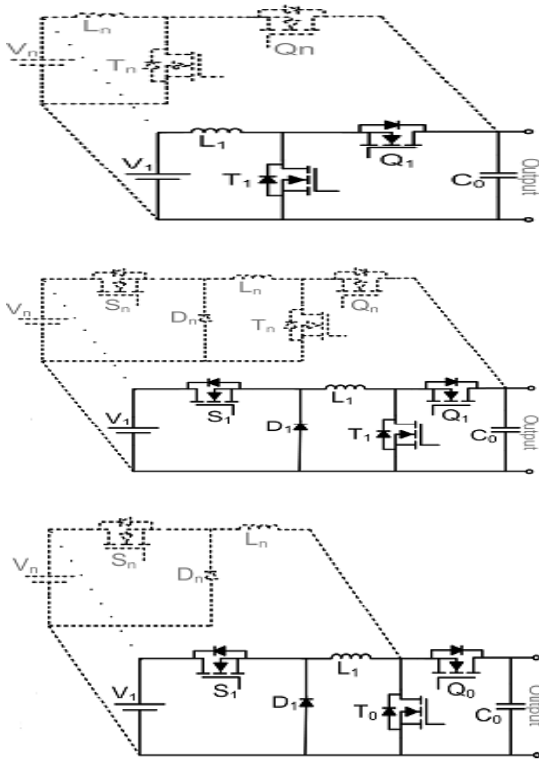
Fig. 1. Bidirectional multi input dc/dc converters. a) Mutiple-input power electronics converter (MIPEC), b) Modified cascaded buck-boost converter (CBBC) approach, c) Proposed converter

A bidirectional MIC called multiple input power electronics converter (MIPEC) whose input ports connected to dc bus via half bridges as shown in Fig.1(a); it can successfully control charge/discharge currents of input

sources whose voltages are required to be less than the output voltage.

A non-isolated unidirectional double input dc-dc power converter is proposed. In boost converter inductor is replaced with a coupled inductor and a high valued capacitor; here, the input current ripple is aimed to be eliminated via a single switch driving the input source energy and energy stored in the capacitor. In this paper, the high valued capacitor is replaced with an EES element, namely a UC, which is essentially a capacitor with large capacitance. This converter is then modified by replacing its output diode with a switch in [25] for battery/UC hybridization for an EV application.

II. A COMPARATIVE ANALYSIS

The proposed bidirectional non-isolated dc-dc converter topology in this work and its counterparts are shown in Fig. 1 As can be seen from this table, MIPEC illustrated in Fig. 1(a) provides boost and buck operations during propulsion and regenerative braking, respectively. The topology given in Fig 1(b) basically consists of modified version of separate cascaded buck-boost converters (CBBC) branches that are connected in parallel. Note that the modified CBBC is considered here for the sake of fair comparison in terms of active switch count.

The proposed converter in this paper which is given in Fig. 1(c)

.

TABLE I
Comparison of Bidirectional Multi-Input Converters

			MIPEC	Modified CBBC approach	proposed
Operation mode during propulsion/reg. braking			Boost/buck	Buck*-boost**/buck	Buck-boost/buck
Number of active switches(n is number of output)			$2*n$	$3*n$	$2+n$
Switch stresses during propulsion /reg. braking	S_i	vol	-	v_i	v_i
		Cur.	-	$\alpha \frac{v_i}{v_0} p.u.l$ $\frac{v_o}{v_i} p.u$	$\frac{1}{d_{si}}$ p.u.l $\frac{v_o}{v_i} p.u$
	$T_0 \; and$ T_i	vol	v_0	v_0	v_0
		Cur.	$1 \, p.u.l$ $\frac{v_o}{v_i} p.u$	$\beta \, p.u.l$ $\frac{v_o}{v_i} p.u$	$\frac{n}{d_{si}}$ p.u.l

(i=1,2,….n)					$n\frac{v_o}{v_i}$ p.u
	T_0 and T_i	Vol.	v_0	v_0	v_0
		Cur.	1 p.u.l $\frac{v_o}{v_i}$ p.u	αp.u.l $\frac{v_o}{v_i}$ p.u	$\frac{n}{d_{yi}}$ p.u.l $n\frac{v_o}{v_i}$ p.u
Overall eff.	1st case : $V_1 = 36V$; $V_2 = 36V$; $V_0 = 48V$.	During prop.	96.02%	95.97%	95.81%@d$_{T0}$=0.25 94.07%@d$_{T0}$=0.5 87.59%@d$_{T0}$=0.75
		During reg.braking	95.88%	94.12%	94.27%
		average	96%	95.71%	95.59%@d$_{T0}$=0.25 94.09%@d$_{T0}$=0.5 88.55%@d$_{T0}$=0.75
	1st case : $V_1 = 60V$; $V_2 = 36V$; $V_0 = 48V$.	During prop.	N/A	95.98%	95.46%@d$_{T0}$=0.25 93.71%@d$_{T0}$=0.5 87.23%@d$_{T0}$=0.75
		During reg.braking		95.39%	95.39%
		average		95.89%	95.45%@d$_{T0}$=0.25 93.97%@d$_{T0}$=0.5 88.39%@d$_{T0}$=0.75
* $\alpha = 1, \beta = 0$ ** $\alpha = \frac{v_o}{v_i}, \beta = 1$,					

All switches in the proposed converter should have same or similar current ratings. In Table I, efficiency comparison of the different converters is given and the switching frequency is 20 kHz and the converters have two input sources.

During the propulsion, the proposed converter exhibits the lowest efficiency, particularly because of increasing switching and conduction losses. During the regenerative braking, the proposed converter is more efficient than the modified CBBC approach since it utilizes fewer active switches thus decreases switching losses.

III. THE ANALYSIS OF THE PROPOSED CONVERTER

The proposed multi-input bidirectional dc-dc converter is analyzed in the case that it has two inputs as illustrated in Fig. 2. As can be seen, the converter has four power switches with internal diodes, two power diodes and two inductors. S1, S2, T0, and Q0 are pulse width modulation (PWM) controlled switches with dS1, dS2, dT0, and dQ0 duty cycles, respectively.
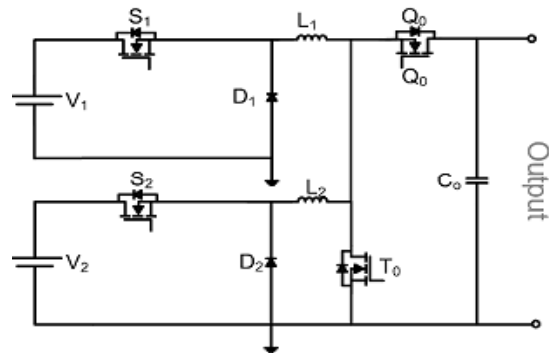

Fig. 2. Proposed multi-input converter with two inputs

The proposed converter has mainly two different operation modes. The first operation mode is called discharging mode. In this mode, the output is fed by input sources according to states of S1, S2 and T0. Power diodes D1 and D2 operate in complementary manner with S1 and S2, respectively.

The second operation mode is called charging mode. In the charging mode, by controlling Q0, regenerative braking energy charges ESSs depending on their voltage levels. The converter operates in continuous conduction mode (CCM).

Discharging Mode

In the discharging mode, one switching cycle consists of four subintervals. Typical waveforms in the discharging mode are illustrated in Fig. 3.

In this figure, it is obvious that dT0<dS2<dS1 according to the assumption that V1< V2<Vo, where V1 is the first input voltage, V2 is the second input voltage, and Vo is the output voltage.
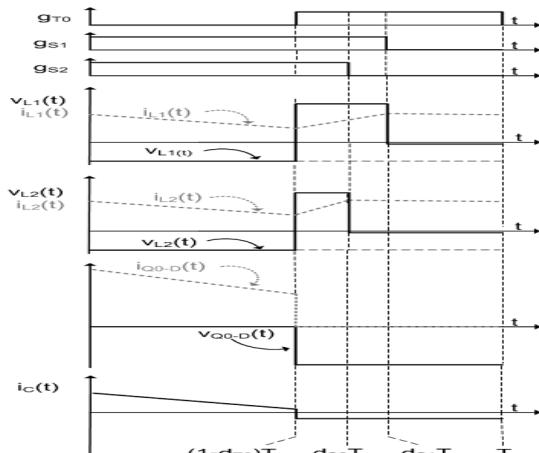
Fig. 3. Typical waveforms in the discharging mode

The relationship between the voltage levels and duty cycles will be explained in detail later on. Steady state equivalent circuits in four subintervals are demonstrated in Fig. 4.

Switching subinterval 1 [0<t<(1-dT0)Ts]: S1 and S2 are turned ON while S0 is turned OFF. D1 and D2 are OFF as shown in Fig. 4(a).
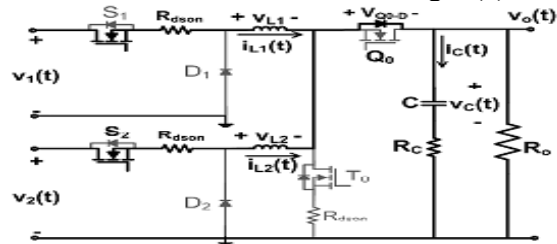
Fig. 4. Equivalent circuits in the discharging mode. (a) Switching subinterval 1: 0<t<(1-dT0)Ts.

Due to the negative voltages across inductors, their currents decrease. In addition, the current through the body diode of Q0 is equal to the sum of inductor currents, and it charges the output capacitor.

Switching subinterval 2 [(1-dT0)Ts<t<dS2Ts]: According to Fig. 4(b), at t=(1-dT0)Ts, T0 is turned ON while S1 and S2 are still conducting, and diodes D1 and D2 are still OFF.
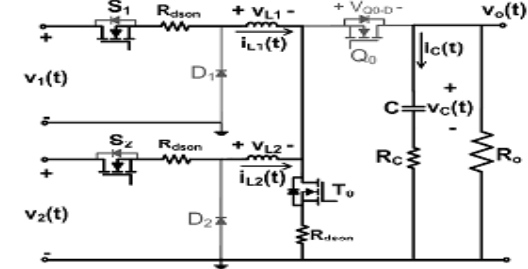

Fig. 5. Equivalent circuits in the discharging mode. (b) Switching subinterval 2: (1-dT0)Ts<t<dS2Ts.

In this subinterval, inductors start to be charged due to positive voltage while the output capacitor discharges to feed the load.

Switching subinterval 3 [dS2Ts<t<dS1Ts]:

At t= dS2Ts, S2 is turned OFF whereas S1 and T0 are still ON. In this subinterval, D2 starts to conduct as shown in Fig. 4(c).
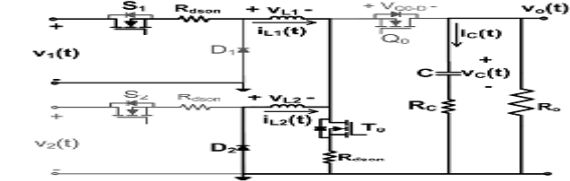

Fig. 6. Equivalent circuits in the discharging mode. (c) Switching subinterval 3: dS2Ts<t<dS1Ts.

As can be seen, L1 current starts to decrease slowly due to the turn-on resistance of T0. Besides, L1 continues to be charged, D1 is still OFF, and output capacitor still discharges.

Switching subinterval 4 [dS1Ts<t<Ts]:

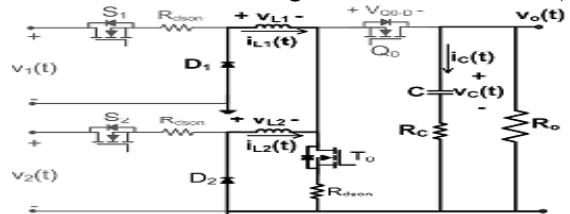Last switching subinterval is initiated by turning OFF S1 at t=dS1Ts as demonstrated in Fig. 4(d).

Fig. 7. Equivalent circuits in the discharging mode. (d) Switching subinterval 4: dS1Ts<t<Ts

Both D1 and D2 become conducting and both inductor currents are decreasing because of the turn on resistance of S0. Moreover, the output capacitor current is still negative.

Finally, equations that show voltage variations of L1 and L2 in the discharging mode can be written as given in (1) and (2), respectively

$$V_{L1}(t) = \begin{cases} V_1(t) - V_0(t) - R_{dson}i_{L1}(t), \\ \quad 0 < t < (1 - V_{T0}(t))T_s \\ V_1(t) - R_{dson}(2i_{L1}(t) + i_{L2}(t)) \\ \quad (1 - d_{T0})T_s < t < d_{s1}T_s \\ -R_{dson}(i_{L1}(t) + i_{L2}(t)) \\ \quad d_{s1}T_s < t < T_s \end{cases} \quad (1)$$

$$V_{L2}(t) = \begin{cases} V_2(t) - V_0(t) - R_{dson}i_{L2}(t), \\ \quad 0 < t < (1 - d_{T0})T_s \\ V_2(t) - R_{dson}(i_{L1}(t) + 2i_{L2}(t)) \\ \quad (1 - d_{T0})T_s < t < d_{s2}T_s \\ -R_{dson}(i_{L1}(t) + i_{L2}(t)) \\ \quad d_{s2}T_s < t < T_s \end{cases} \quad (2)$$

The output capacitor current and output voltage variations depending on the state of the S0 can be derived as given in (3) and (4).

$$i_C(t) = \begin{cases} \frac{R_0(i_{L1}(t) + i_{L2}(t))}{R_0 + R_C} - \frac{1}{R_0 + R_C}V_C(t), 0 < t < (1 - d_{T0})T_s \\ -\frac{1}{R_0 + R_C}V_C(t) \quad (1 - d_{T0})T_s < t < T_s \end{cases}$$
$$(3)$$

$$V_0(t) = \begin{cases} \frac{R_0 R_C}{R_0 + R_C}(i_{L1}(t) + i_{L2}(t)) + \frac{R_0}{R_0 + R_C}V_C(t), \\ \quad 0 < t < (1 - d_{T0})T_s \\ -\frac{R_0}{R_0 + R_C}V_C(t) \quad (1 - d_{T0})T_s < t < T_s \end{cases} \quad (4)$$

The relationship between the output voltage and source voltages at steady state can be obtained as given in (5) by neglecting Rdson.

$$V_0 = V_1 \frac{d_{s1}}{1 - d_{T0}} = V_2 \frac{d_{s2}}{1 - d_{T0}} \quad (5)$$

According to (5), the converter operates at an equilibrium point where duty cycles have following relationship:

$$\frac{V_1}{V_2} = \frac{d_{s1}}{d_{s2}} \quad (6)$$

Charging Mode

In the charging mode, Q0 is controlled and T0 is kept OFF in order to store regenerative braking energy into the energy storage units while regulating the output voltage. As expressed, charging only one ESS can be realized by adding a solid-state switch to the converter input.
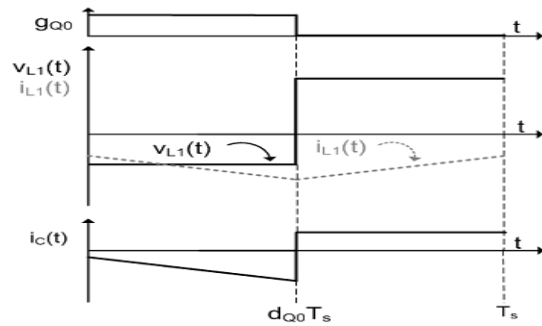

Fig. 8. Typical waveforms in the charging mode

Fig. 8 illustrates the steady state waveforms in the charging mode. According to this figure, one switching cycle is composed of two subintervals. Associated equivalent circuits are shown in Fig.6 where ireg(t) is the current source that represents the regenerative braking energy. In this mode, the inductor current is negative since the source is charged.

Switching subinterval 1 [0<t<dQ0Ts]:

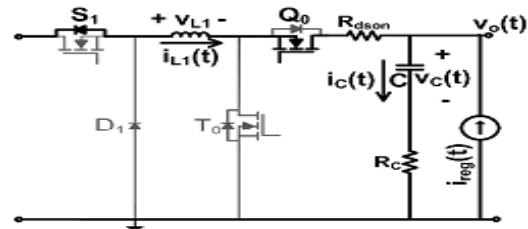From Fig. 6(a) one can see that, when Q0 is turned ON, the body diode of S0 becomes OFF.

Fig. 9. Equivalent circuits in charging mode. (a) Switching subinterval 1: 0<t<dQ0Ts.

Because of negative voltage across L1, its current increases (negatively). Moreover, the current of the output capacitor is negative since it discharges.

Switching subinterval 2 [dQ0Ts<t<Ts]:

At t=dQ0Ts, Q0 is turned OFF. Therefore, the current of L1 now flows through T0 body diode as illustrated in Fig. 6(b). In this subinterval, the inductor current decreases due to the source voltage across it. Additionally, the current of output capacitor changes its direction and becomes positive.
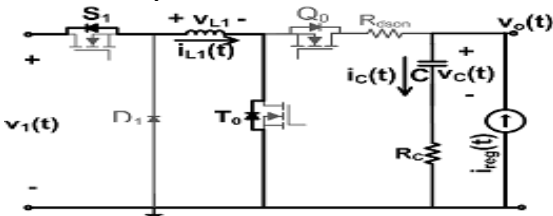

Fig. 10. Equivalent circuits in charging mode. ((b) Switching subinterval 2: dQ0Ts<t<Ts.

Based on the analysis above, the equations for the L1 voltage, output capacitor current, and output voltage in two switching subintervals can be given as given in (7), (8), and (9), respectively.

$$v_{L1}(t) = \begin{cases} V_1(t) - V_0(t) - R_{dson}i_{L1}(t), 0 < t < d_{Q0}T_s \\ V_1(t), \quad d_{Q0}T_s < t < T_s \end{cases} \quad (7)$$

$$i_C(t) = \begin{cases} i_{L1}(t) + i_{reg}(t), 0 < t < d_{Q0}T_s \\ i_{reg}(t), \ d_{Q0}T_s < t < T_s \end{cases} \quad (8)$$

$$V_0(t) = \begin{cases} \big(i_{L1}(t) + i_{reg}(t)\big)R_C + V_C(t), 0 < t < (1-d_{T0})T_s \\ i_{reg}(t)R_C + V_C(t), \ d_{Q0}T_s < t < T_s \end{cases}$$

$$(9)$$

Applying to small ripple approximation and inductor volt second-balance to (7), one can find the relationship between the output voltage (Vo) and source voltage (V1) at steady state as in (10) by neglecting Rdson.

$$V_0 = \frac{V_1}{d_{Q0}} \quad (10)$$

IV. SMALL SIGNAL MODELING AND CONTROLLER CONSIDERATIONS

Small Signal Modeling

A single controller can be used for buck mode (charging) and boost mode (discharging) of a bidirectional converter; and that controller can be designed according to one of the transfer functions of these two operating modes. Therefore, in this paper, a classical boost converter is analyzed for the charging mode.

A small signal ac model in matrix form can be given in (11) where A, B, and C are matrices comprised of constants

$$A\hat{x}(s) = B\hat{d}(s) + C\hat{v}(s) \quad (11)$$

In (11), x(s), d(s), and v(s) denote the state variables, duty cycles, and input voltages, respectively, which consist of dc components (X, D, and V) and small perturbations (x(s) , d(s) , and v (s)) as shown in (12).

$$x = X + \hat{x}(s) \quad d = D + \hat{d}(s) \quad v = V + \hat{v}(s) \quad (12)$$

Control Strategy

A battery/UC HESS is considered here in order to test the proposed converter, and the control strategy which is demonstrated in Fig. 7 is applied to system.
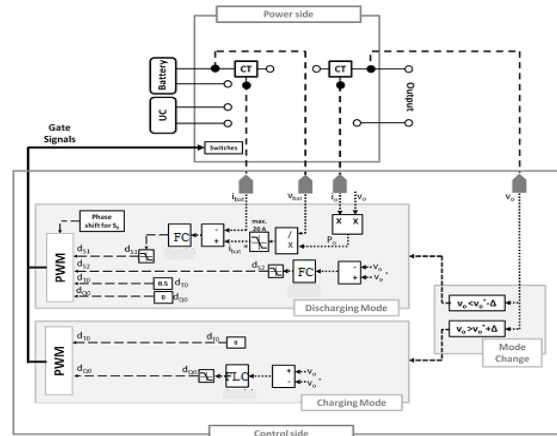

Fig. 11. Overall control strategy

In this figure, the power side represents the proposed power converter where CT denotes current transducers. In addition, the control side is the platform where currents and voltages are sensed and developed control strategy is carried out. In the control side, first of all, the operation mode is determined by checking the output voltage (vo): the discharging mode is activated when vo is lower than vo*-Δ and the charging mode is activated when vo is greater than vo*+Δ, where vo* is the output voltage reference and Δ is a defined voltage level.

In the discharging mode, it is aimed to realize active power sharing between battery and UC. In order to achieve this, a fuzzy controller adjusts the duty cycle of S1 to control the battery power while another fuzzy controller adjusts the duty cycle of S2 for dc bus regulation.

Controller Design

Transfer function matrices can be obtained by solving small signal model in (11) for each operation mode as given in (15).

$$\hat{x}(s) = A^{-1}B\hat{d}(s) + A^{-1}C\hat{v}(s) \quad (13)$$

If the effect of cross-coupling transfer functions in (15) is assumed to be negligible, decoupled transfer function can be derived.

$$\frac{i_{bat}(s)}{\hat{d}_{s1}(s)} = \frac{i_{L1}(s)}{\hat{d}_{s1}(s)}D_1 + I_{L1} \quad (14)$$

Using (15), the coefficients for both operation modes can be calculated as given in Table II and Table III

$$G(s) = \frac{b_0 + b_1 s + b_2 s^2}{a_0 + a_1 s + a_2 s^2} \quad (15)$$

Fig.8 & Fig.9 demonstrate the uncompensated and compensated system bode plots for the discharging and charging modes, respectively.
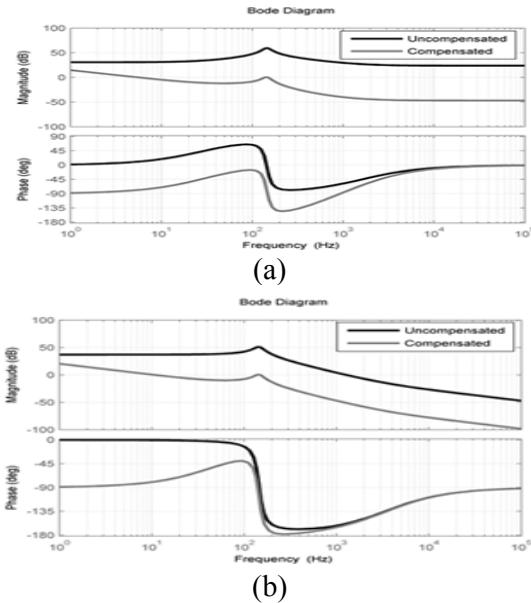
(a)

(b)

Fig. 12. Bode plots of discharging mode (a) $\hat{i}_{s1}(s)/\hat{d}_{s1}(s)$ and (b) $\hat{v}_0(s)/\hat{d}_{s2}(s)$
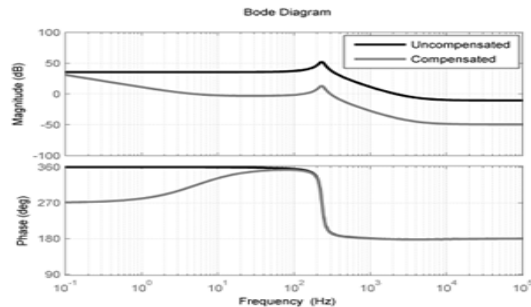

Fig. 13. Bode plot of charging mode: $\hat{v}_0(s)/\hat{d}_{Q0}(s)$

From these figures it can be seen that, all of the compensated systems have positive phase margins hence they are stable.

Table II
Discharging Mode Transfer Function Coefficients

	$\hat{i}_{bat}(s)/\hat{d}_{s1}(s)$	$\hat{v}_o(s)/\hat{d}_{S2}(s)$
a_0	$D_{T0}^{'2}R_o + (D_{T0} + D_{S1})R_{dson}$	
a_1	$L_{1,2} + (R_o + R_c)(D_{T0} + D_{S1})(R_{dson} + D_{T0}^{'2}R_oR_c)C$	
a_2	$(R_C + R_o)L_{1,2}C$	
b_0	$D_{S1}(V_{bat} - I_{L1}R_{dson}) + I_{L1}a_0$	$D_{T0}^{'}(V_{UC} - I_{L2}R_{dson}) \times \left(\dfrac{R_o^2}{R_o + R_C} + \dfrac{R_C}{R_o + R_C} \right)$
b_1	$D_{S1}(V_{bat} - I_{L1}R_{dson})(R_C + R_o)C + I_{L1}a_1$	$D_{T0}^{'}(V_{UC} - I_{L2}R_{dson})(R_oR_cC)$
b_2	$I_{L1}a_2$	0

Table III
Charging Mode Transfer Function Coefficients

	$\hat{v}_0(s)/\hat{d}_{Q0}(s)$
a_0	$D_{Q0}^2R_0 + D_{Q0}R_{dson}$
a_1	$L_2 + (R_c + R_0)D_{Q0}(R_{dson} + D_{Q0}C)$
a_2	$(R_c + R_0)L_2C$
b_0	$V_0D_{Q0}R_0 - I_{L_2}R_0R_{dson}D_{Q0}$
b_1	$V_0D_{Q0}R_0R_cC - I_{L_2}R_0(L_2 + D_{Q0}R_{dson}R_cC)$
b_2	$-I_{L_2}R_0R_cL_2C_0$

Moreover, decreased cut-off frequencies result in low gain in high frequencies; therefore, increase the robustness [17]. Note that parameters given in Table V are utilized to derive bode plots and design the controllers.

Table IV
Controller Parameters

	Discharging mode		Charging
	$G_{PI-1}(S)$	$G_{PI-2}(S)$	$G_{PI-3}(S)$
K_P	0.000291	0.00278	0.011414
K_i	0.98979	0.92074	0.37555

Table V
Bode Plot Parameters

V_0	48V
$V_{bat} = V_{UC}$	36V
$L_1 = L_2$	$150\mu H$
R_0	4.6Ω
R_{down}	$3.8\,m\Omega$
R_c	$23\,m\Omega$
D_{S0}	0.5
D_{S1}	0.67
D_{Q0}	0.25

V. FUZZY LOGIC CONTROLLER

In FLC, basic control action is determined by a set of linguistic rules. These rules are determined by the system. Since the numerical variables are converted into linguistic variables, mathematical modeling of the system is not required in FC.
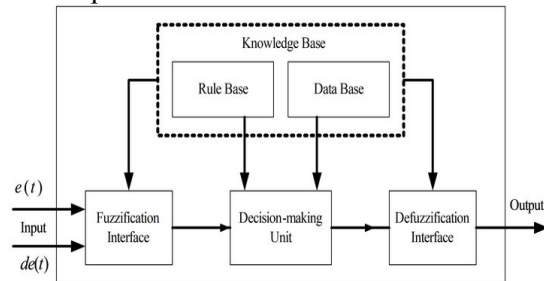

Fig:14. Fuzzy logic controller

According to the fig :10 which shown the block diagram of fuzzy logic controller . here FLC comprises of three parts: fuzzification, interference engine and defuzzification. The FC is characterized as i. seven fuzzy sets for each input and output. ii. Triangular membership functions for simplicity. iii. Fuzzification using continuous universe of discourse. iv. Implication using Mamdani's, 'min' operator. v. Defuzzification using the height method.

TABLE VI: Fuzzy Rules

Change in error	ERROR						
	NB	NM	NS	ZO	PS	PM	PB
NB	NB	NB	NM	NS	NS	ZO	ZO
NM	NB	NB	NM	NS	NS	ZO	ZO
NS	NB	NM	NS	NS	ZO	PS	PS
ZO	NM	NM	NS	ZO	PS	PM	PM
PS	NM	NS	ZO	PS	PS	PM	PB
PM	ZO	ZO	PS	PS	PM	PB	PB
PB	ZO	ZO	PS	PM	PM	PB	PB

Fuzzification: Membership function values are assigned to the linguistic variables, using seven fuzzy subsets: NB (Negative Big), NM (Negative Medium), NS (Negative Small), ZE (Zero), PS (Positive Small), PM (Positive Medium), and PB (Positive Big). The Partition of fuzzy subsets and the shape of membership CE(k) E(k) function adapt the shape up to appropriate system. The value of input error and change in error are normalized by an input scaling factor.In this system the input scaling factor has been designed such that input values are between -1 and +1. The triangular shape of the membership function of this arrangement presumes that for any particular E(k) input there is only one dominant fuzzy subset. The input error for the FLC is given as

$$E(k) = \frac{P_{ph(k)} - P_{ph(k-1)}}{V_{ph(k)} - V_{ph(k-1)}} \qquad (16)$$

$$CE(k) = E(k) - E(k-1) \qquad (17)$$

Inference Method: Several composition methods such as Max–Min and Max-Dot have been proposed in the literature. In this paper Min method is used. The output membership function of each rule is given by the minimum operator and maximum operator. Table 1 shows rule base of the FLC.

Defuzzification: As a plant usually requires a non-fuzzy value of control, a defuzzification stage is needed. To compute the output of the FLC, „height" method is used and the FLC output modifies the control output. Further, the output of FLC controls the switch in the inverter. In UPQC, the active power, reactive power, terminal voltage of the line and capacitor voltage are required to be maintained. In order to control these parameters, they are sensed and compared with the reference values. To achieve this, the membership functions of FC are: error, change in error and output The set of FC rules are derived from

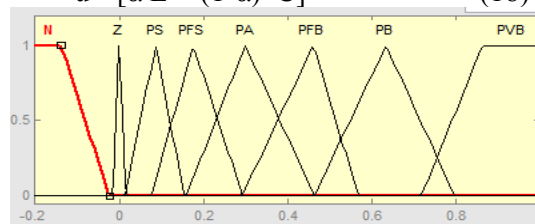$$u = -[\alpha E + (1-\alpha)*C] \qquad (18)$$
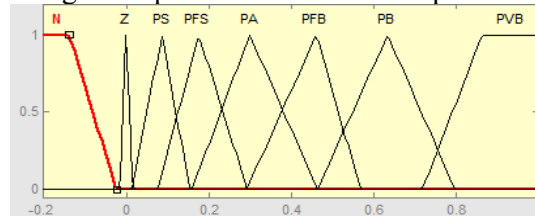

Fig :11 input error as membership functions

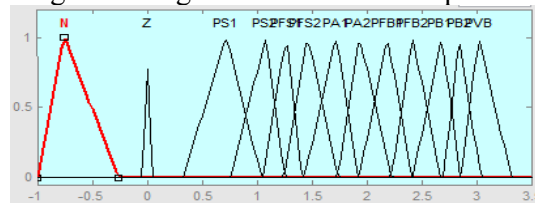Fig: 12 change as error membership functions

Fig:13 output variable Membership functions

Here figure: 11, 12 and 13 show the member function of the input error, change as error and output variable function.Where α is self-adjustable factor which can regulate the whole operation. E is the error of the system, C is the change in error and u is the control variable. And figure :14 simulation block of fuzzy logic controller.
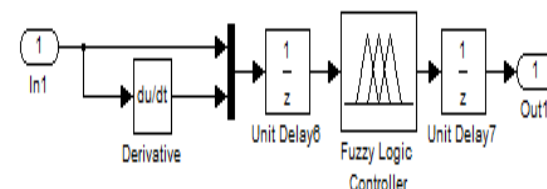

Fig :15 Fuzzy logic controller in simulation

VI. SIMULATION RESULTS

In order to verify the analysis and evaluate the dynamic performance of the converter. Fig: 15 show the block diagram of proposed system. Fig: 16 which show the control diagram of the proposed system which shown below.
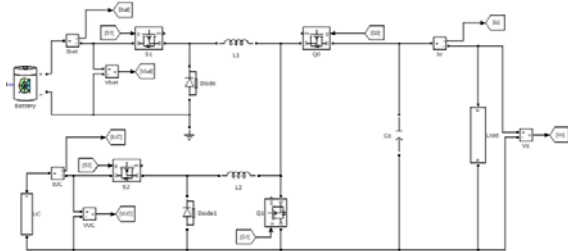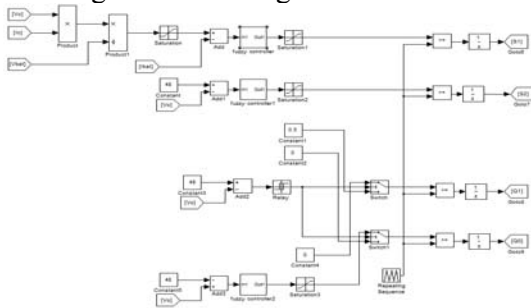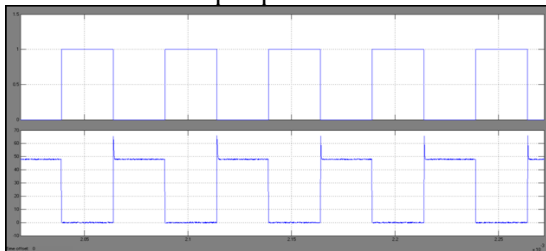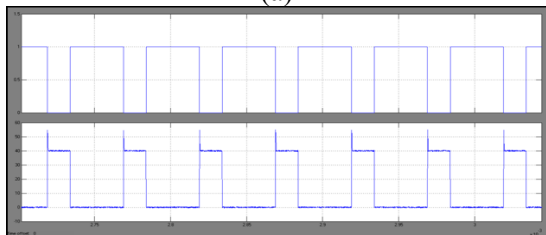

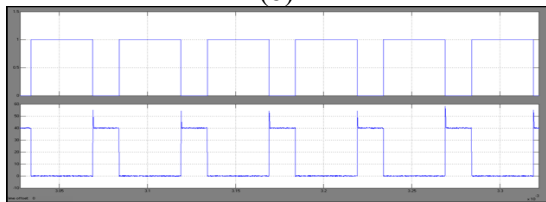Fig:16 Block diagram of simulation

Fig:16 Control block diagram of simulation

Figs. 17-19 demonstrate the measured steady state waveforms for the discharging mode when the output power is set to 400 W.

(a)

(b)

(c)

Fig. 17. Simulation waveforms of switches gate-source and drain-source voltages in discharging mode: (a) S0: vGS-T0 [Ch1: 5V/div], vDS-T0 [Ch2: 30V/div). (b) S1: vGS-S1 [Ch1: 5V/div], vDS-S1 [Ch2: 20V/div]. (c) S2: vGS-S2 [Ch1: 5V/div], vDS-S2 [Ch2: 20V/div]. Time base: 20µs/div.

Fig.18 illustrates L1 and L2 voltage and current variations. Inductor voltages and inductor currents vary according to states of switches. Moreover, both inductor currents are positive since both energy storage elements discharge.
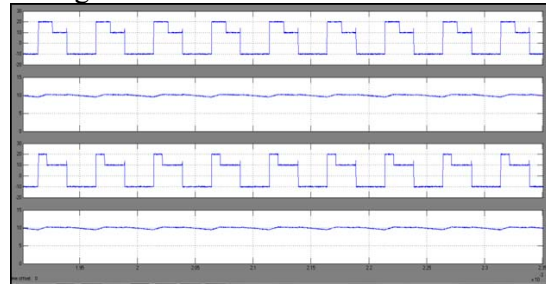

Fig. 18. Simulation waveforms of inductor voltages and currents in the discharging mode: L1: vL1 [Ch1: 40 V/div], iL1 [Ch3: 5 A/div], L2: vL2 [Ch2: 40 V/div], iL2 [Ch4: 5 A/div]. Time base: 20 µs/div

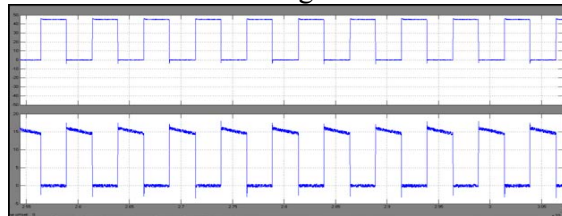The voltage and current of Q0 body diode are illustrated in Fig.19.

Fig. 19. Simulation waveforms of Q0 switch body diode voltage and current in the discharging mode: vQ0-D [Ch1: 20V/div], iQ0-D [Ch3:10A/div]. Time base: 20µs/div

From Fig.19 and Fig.17, one can see that when T0 is OFF, the diode starts to conduct as can be understood from its positive current. Conversely, when S0 is ON, the diode becomes OFF thus its current goes to zero.
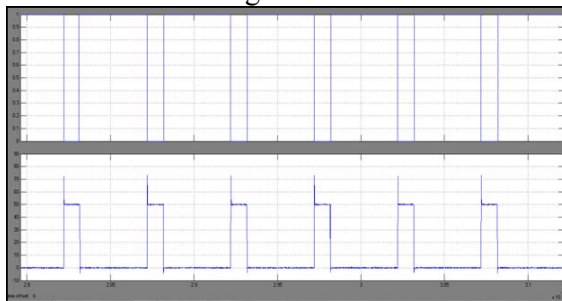

Fig. 20.Simulation waveforms of switch Q0 gate-source and drain-source voltages in the discharging mode: (a) vGS-Q0 [Ch1: 5V/div], vDS-Q0 [Ch2: 20V/div). Time base: 20µs/div.

Figs. 20-21 illustrate the measured steady state waveforms when the converter operates in the charging mode.
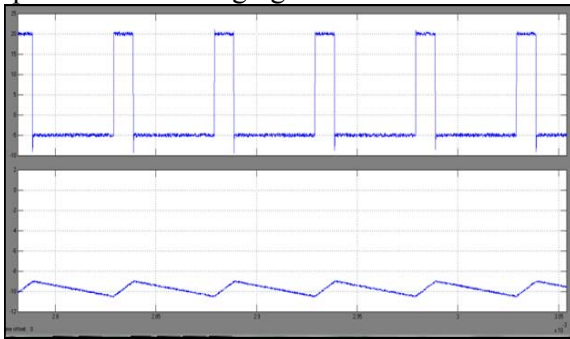

Fig.21. Simulation waveforms of inductor voltage and current in the charging mode: vL2 [Ch1: 20V/div], iL2 [Ch3: 3A/div]. Time base: 20µs/div.

In Fig. 21, the voltage and current variations of L2 are demonstrated. It can be noticed that the inductor current is negative since UC is charged. Moreover, when Q0 is turned ON, the voltage of the inductor becomes negative thus its current increases (negatively); conversely, turning it OFF makes the voltage of the inductor equal to UC voltage and decreases its current (negatively).
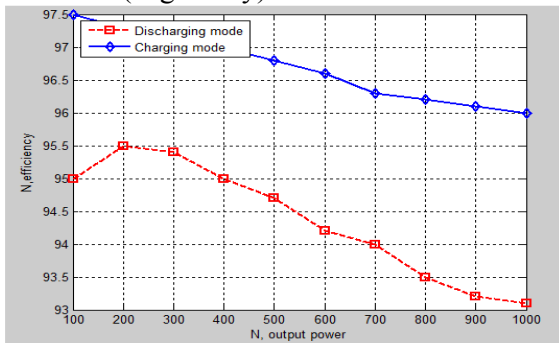

Fig.22. Efficiency curves

Fig. 22 illustrates the proposed converter efficiency curves for the discharging and charging modes which are obtained by power analyzer.
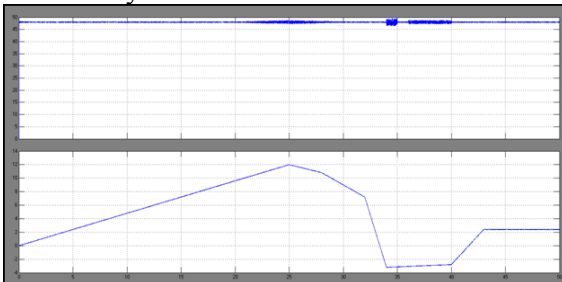

Fig.23. Dynamic test results: a) output voltage, b) output current.

In Fig. 23, the output voltage and output current are shown. Here, it is clear that the output voltage is successfully regulated at 48 V in both cases. Fig. 24 shows the battery and UC average current.
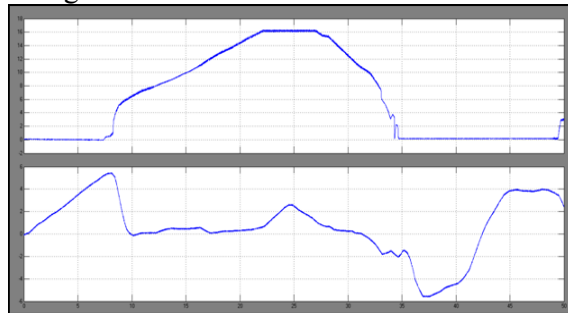

Fig.24. Dynamic test results: a) battery current, b) UC average current.

In both cases maximum battery current is limited to 20 A due to the control strategy; at this instant, UC current is increased for compensating the load demand. Additionally, UC current becomes negative when it stores regenerative braking energy.
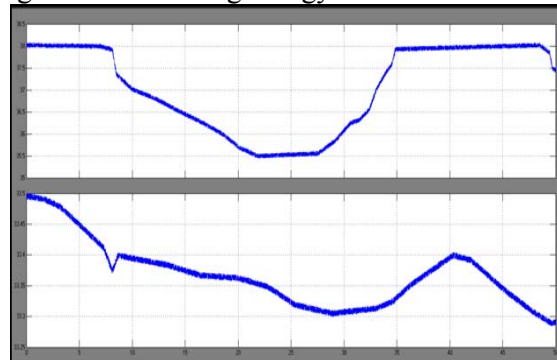

Fig.25. Dynamic test results: a) battery voltage, b) UC voltage.

Fig. 25 highlights the input source voltages. In addition to that, UC voltage decreases when it compensates load demand and increases when it is charged.

CONCLUSION

In this paper we are implementing a new multi input non isolated bidirectional dc/dc converter which is utilized for the electric vehicle application. Here we are using the fuzzy controller. Fuzzy controller is the combination of fuzzification, interference method and defuzzification which is based upon the rules. There are different types of operation mode used for the proposed system. Therefore due to battery/UC hybrid system this is associated with the transfer function which is developed by the battery current and regulating output voltage. Here we are utilizing the fuzzy controller for a nonlinear system allows for a reduction of

uncertain effects in the system control and improve the efficiency. By using the simulation results we can analyze the novel bidirectional non-isolated multi-input converter (MIC) topology for hybrid systems to be used in electric vehicles.

REFERENCES

[1] S. M. Lukic, R. C. Bansal, F. Rodriguez, and A. Emadi, "Energy Storage Systems for Automotive Applications," IEEE Trans. Ind. Electron., vol. 55, no. 6, pp. 2258–2267, Jun. 2008.

[2] O. C. Onar, J. Kobayashi, and A. Khaligh, "A Fully Directional Universal Power Electronic Interface for EV, HEV, and PHEV Applications," IEEE Trans. Power Electron., vol. 28, no. 12, pp. 5489– 5498, Dec. 2013.

[3] A. Khaligh, "Battery, Ultracapacitor, Fuel Cell, and Hybrid Energy Storage Systems for Electric, Hybrid Electric, Fuel Cell, and Plug-In Hybrid Electric Vehicles: State of the Art," IEEE Trans. Veh. Technol., vol. 59, no. 6, pp. 2806–2814, 2010.

[4] S. Dusmez, A. Hasanzadeh, and A. Khaligh, "Comparative Analysis of Bidirectional Three-Level DC–DC Converter for Automotive Applications," IEEE Trans. Ind. Electron., vol. 62, no. 5, pp. 3305– 3315, May 2015.

[5] J. Shen, S. Dusmez, and A. Khaligh, "Optimization of Sizing and Battery Cycle Life in Battery/Ultracapacitor Hybrid Energy Storage Systems for Electric Vehicle Applications," IEEE Trans. Ind. Informatics, vol. 10, no. 4, pp. 2112–2121, Nov. 2014.

[6] S. Lu, K. A. Corzine, and M. Ferdowsi, "A New Battery/Ultracapacitor Energy Storage System Design and Its Motor Drive Integration for Hybrid Electric Vehicles," IEEE Trans. Veh. Technol., vol. 56, no. 4, pp. 1516–1523, Jul. 2007.

[7] S. Dusmez and A. Khaligh, "A Supervisory Power-Splitting Approach for a New Ultracapacitor–Battery Vehicle Deploying Two Propulsion Machines," IEEE Trans. Ind. Informatics, vol. 10, no. 3, pp. 1960–1971, Aug. 2014.

[8] Z. Ding, C. Yang, Z. Zhang, C. Wang, and S. Xie, "A novel softswitching multiport bidirectional dc-dc converter for hybrid energy storage system," IEEE Trans. Power Electron., vol. 29, no. 4, pp. 1595– 1609, 2014

[9] H. Zhou, T. Bhattacharya, D. Tran, T. S. T. Siew, and A. M. Khambadkone, "Composite energy storage system involving battery and ultracapacitor with dynamic energy management in microgrid applications," IEEE Trans. Power Electron., vol. 26, no. 3, pp. 923–930, 2011.

[10] S. Dusmez, S. Member, X. Li, S. Member, B. Akin, and S. Member, "A New Multiinput Three-Level DC / DC Converter," vol. 31, no. 2, pp. 1230–1240, 2016.

[11] K. Colak, E. Asa, M. Bojarski, and D. Czarkowski, "Asymmetrical Duty-Cycle Control of a Novel Multi- Port CLL Resonant Converter," vol. 3, no. 4, pp. 3019–3024, 2015.

[12] S. Lu, K. A. Corzine, and M. Ferdowsi, "A Unique Ultracapacitor Direct Integration Scheme in Multilevel Motor Drives for Large Vehicle Propulsion," IEEE Trans. Veh. Technol., vol. 56, no. 4, pp. 1506–1515, Jul. 2007.

[13] M. B. Camara, H. Gualous, F. Gustin, A. Berthon, and B. Dakyo, "DC / DC Converter Design for Supercapacitor and Battery Power Management in Hybrid Vehicle Applications — Polynomial Control Strategy," IEEE Trans. Ind. Electron., vol. 57, no. 2, pp. 587–597, 2010.

[14] S. K. Kollimalla, M. K. Mishra, and N. L. Narasamma, "Design and Analysis of Novel Control Strategy for Battery and Supercapacitor Storage System," IEEE Trans. Sustain. Energy, vol. 5, no. 4, pp. 1137– 1144, Oct. 2014.

[15] A. Tani, M. B. Camara, and B. Dakyo, "Energy management based on frequency approach for hybrid electric vehicle applications: Fuelcell/lithium-battery and ultracapacitors," IEEE Trans. Veh. Technol., vol. 61, no. 8, pp. 3375–3386, 2012.